AIAA JOURNAL
Vol. 30, No. 4, April 1992

Optimization of Bluff Body for Minimum Drag in Ground Proximity

T. Han,* D. C. Hammond Jr.,† and C. J. Sagi‡
General Motors Research Laboratories, Warren, Michigan 48090

Three-dimensional Navier-Stokes analysis was applied to optimize the rear-end shape of a vehicle-like body in ground proximity. The flow analysis was coupled with an optimization program to find values of the shape parameters (backlight angle, boat-tail angle, and ramp angle) that produce a minimum aerodynamic drag coefficient. The approach of this method is to create a localized quadratic approximation to the objective function, in this case, drag coefficient, in terms of the three shape parameters. Values of the objective function are calculated using Navier-Stokes analysis of proposed optimum geometries; the localized objective function approximation is updated and used to select a new geometry, and the iteration process is repeated until the objective function converges to a minimum value. The optimum design geometry (17.8-deg backlight, 18.9-deg boat tail, 9.2-deg ramp) was obtained after 15 Navier-Stokes analyses. The predicted drag coefficient reduction was 0.10 referenced to the constant-cross-section afterbody. It was observed that the optimum afterbody shape minimized the trailing vortices in the wake and also produced near zero afterbody lift force. The experimentally determined optimum, for a similar body, was very flat but fell in the range of 15- −18-deg backlight, 15- −22-deg boat tail, and 9- −14-deg ramp. The measured drag coefficient reduction was 0.13.

Introduction

REDUCING the drag on bluff bodies in ground proximity has important practical applications to ground vehicles. In contrast to the situation in aeronautics, where flow separation from body surfaces is largely avoided, ground vehicles inherently exhibit significant regions of flow separation of both quasi-two-dimensional and fully three-dimensional character. Most of the drag on bluff bodies is pressure drag, directly due to flow separation from the body surface. Therefore, minimizing the drag of bluff bodies is an exercise in controlling the location and scale of unavoidable flow separations.

It is often observed that the drag coefficient is not sensitive to the forebody shape if the flow over that region is free from large-scale separations.[1] (Traditionally, on automobiles, the forebody is that portion ahead of, and the afterbody that portion behind, the transverse plane of maximum cross-sectional area. On bluff bodies like the one considered here, the exact division is unclear and unimportant.) By careful body shaping, flow separation on the forebody can be easily minimized for the turbulent flows usually experienced. In contrast, flow separation on the afterbody of ground vehicles is unavoidable and much less controllable. Separation on the afterbody is the major source of aerodynamic drag for bluff bodies (with separation-free forebodies). Therefore, reducing the aerodynamic drag produced by the afterbody becomes one of the most important subjects in ground vehicle aerodynamics.

Boat tailing is a well-known method of drag reduction and has been applied to two-dimensional and axisymmetric bodies[2] as well as three-dimensional vehicle-like bluff bodies. By tapering the afterbody surface, boat tailing permits pressure recovery in the flow along the afterbody surface, thereby reducing the pressure drag. Excessive boat tailing produces flow separation and can even increase drag above that of the unboat-tailed geometry. Three independent boat-tailing angles (upper, side, and lower surfaces) are required to specify the geometry of three-dimensional bluff bodies with rectangular cross sections. These three angles are called the backlight angle, boat-tail angle, and ramp angle and are shown in Fig. 1. In addition to the quasi-two-dimensional separation that can occur on two-dimensional boat-tailed bodies, three-dimensional bodies can exhibit three-dimensional separation, i.e., vortex shedding from longitudinal edges. This results from flow interaction among upper, side, and lower surfaces that is complex and highly nonlinear.

Heretofore, afterbody shape optimization has relied heavily on wind-tunnel testing.[3] This paper reports a computational technique for optimizing afterbody shape to minimize drag.

Previous Computational Study of Ahmed's Body

Computations were previously performed for three-dimensional turbulent flows around Ahmed's vehicle-like body.[4] The detailed computational method and results were reported for various afterbody backlight angles for a pure fastback afterbody at a Reynolds number of 4.3×10^6 based on body length.[5] This previous computational study predicted most of the essential measured features of the flowfield around Ahmed's body in ground proximity, such as the formation of trailing vortices and flow separation with recirculation at the vertical base of the afterbody. It also established that the incremental changes in the drag coefficient produced by changes in backlight angle were predicted with reasonable accuracy for the backlight angles between 0 and 25 deg. This quantitative validation prompted the exploration of the use of the analysis for aerodynamic optimization.

Solution Procedure

The previously validated three-dimensional Navier-Stokes analysis with a standard k-ϵ turbulence model, VINE3D,[5] was manually coupled with a parametric optimization analysis, COPES,[6] and used to find the optimum afterbody shape design variables (backlight angle, boat-tail angle, and ramp angle) that

Presented as Paper 90-3027 at the AIAA 8th Applied Aerodynamics Conference, Portland, OR, Aug. 20–22, 1990; received Sept. 19, 1990; revision received May 15, 1991; accepted for publication May 17, 1991.

*Staff Research Engineer, Engineering Mechanics Department. Member AIAA.

†Senior Staff Engineer, Engineering Mechanics Department; currently, Director of Automotive Marketing, Cray Research, Inc. Member AIAA.

‡Staff Research Engineer, Engineering Mechanics Department; currently, Test Engineer, GM Design Staff.

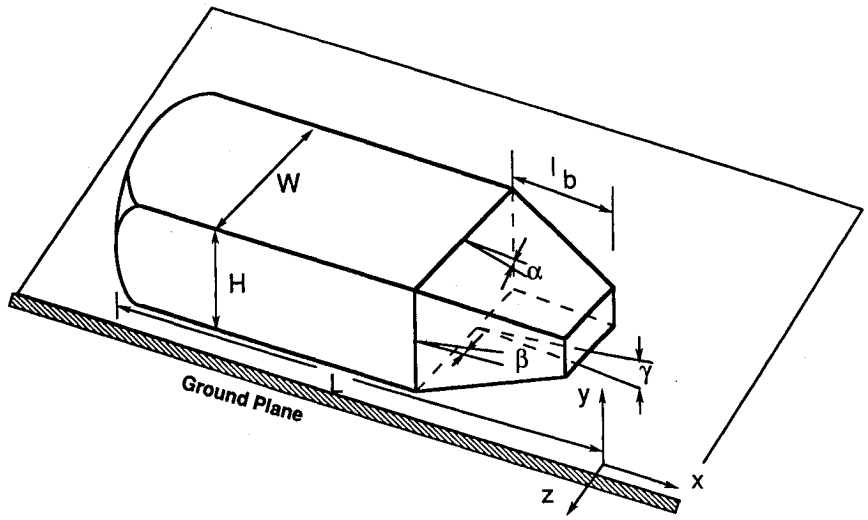

Fig. 1 Schematic of the vehicle-like body with three boat-tail angles in ground proximity.

produce a minimum aerodynamic drag coefficient. The Navier-Stokes analysis used has been fully described by Han[5]; in the interest of brevity, that description will not be repeated here. A brief summary of the optimization analysis follows.

The approximate optimization technique, COPES,[6] is suitable for problems with fewer than 10 design variables and where the computational cost of each analysis is very high. The method used is to create an analytic approximation to the objective function, the drag coefficient in the present study, in terms of the three design parameters (backlight, boat-tail, and ramp angles).[7] We then perform the optimization using these approximations and search for a proposed optimum design. The objective function for the drag coefficient is then updated by including the results of a Navier-Stokes analysis of this proposed optimum design, and the process is continued until convergence to a precise optimum design geometry has been achieved.

The approximate function for the drag coefficient can be obtained by a simple Taylor series expansion:

$$C_D(\boldsymbol{X}) = C_D(\boldsymbol{X}^o) + \Delta C_D(\boldsymbol{X}^o)\delta\boldsymbol{X} + {}^1/_2\delta\boldsymbol{X}\boldsymbol{H}(\boldsymbol{X}^o)\delta\boldsymbol{X} \quad (1)$$

where $\boldsymbol{X}$ is the vector of design variables, three afterbody angles in the present study, and superscript o denotes the nominal design values. $C_D(\boldsymbol{X})$ is the objective function, drag coefficient; $\Delta C_D(\boldsymbol{X})$ is the gradient; and $\boldsymbol{H}(\boldsymbol{X})$ is the Hessian matrix. The perturbation of design variables $\delta\boldsymbol{X}$ is defined as

$$\delta\boldsymbol{X} = \boldsymbol{X} - \boldsymbol{X}^o \quad (2)$$

To have full quadratic approximation of the objective function, we have to determine $m = (n + 3)n/2$ unknowns where n is the number of design parameters ($n = 3$ and $m = 9$ in the present study) in addition to a nominal design $\boldsymbol{X}^o$.

In the present study, our main objective is to minimize the drag coefficient subject to simple linear constraints of the design variables, i.e.,

Minimize

$$C_D(\alpha,\beta,\gamma)$$

Subject to

$$0 < \alpha < 30 \text{ deg}$$

$$0 < \beta < 30 \text{ deg}$$

$$0 < \gamma < 20 \text{ deg}$$

where α, β, and γ are backlight, boat-tail, and ramp angles, respectively. In the present study, these constraints are specified simply to maintain a positive rear vertical base area and also to avoid the flow separation that was observed from the experiment[4] for boat-tail angles greater than 30 deg. These constraints can be subsequently modified based on specific styling or packaging constraints. $C_D(\alpha,\beta,\gamma)$ is the pressure drag of the afterbody having angles α, β, and γ and is evaluated numerically by solving the Navier-Stokes equations.

Table 1 Taguchi orthogonal arrays

Array	Backlight α	Boat tail β	Ramp γ
1	1	1	1
2	1	2	2
3	1	3	3
4	2	1	2
5	2	2	3
6	2	3	1
7	3	1	3
8	3	2	1
9	3	3	2

Table 2 Design variables

Level	Backlight α, deg	Boat tail β, deg	Ramp γ, deg
1	0	0	0
2	10	10	7
3	25	25	15

The overall accuracy and stability of the optimization depends on how the objective function is approximated and, also, how the objective function spans the design space to include a global optimum. To cover a wide range of the design space, the initial objective function was approximated from an initial distribution of the design variables based on Taguchi orthogonal arrays.[8] The Taguchi orthogonal arrays for three levels and three design parameters are shown in Tables 1 and 2. The three level design values were specified to cover a wide range of design space, i.e., 0, 10, and 25 deg for both backlight and boat-tail angles and 0, 7, and 15 deg for ramp angles.

Present Computational Study

In the present study, the afterbody shape is defined by the three afterbody angles and the length of the afterbody is specified the same as the height of the body ($l_b/H = 1.0$). Therefore, it consists arbitrarily of a forebody, a long midsection, and an afterbody. Again, all computations were based on a

freestream velocity of 60 m/s, which corresponds to a Reynolds number of 4.3×10^6.

Boundary Conditions

Because of the relatively long midsection, the flow interaction between the rear and the front is very weak. It was observed from both experiment and computation that there are no noticeable differences in the surface pressures on the forebody even with large changes in the afterbody. In the present study, the numerical computations were performed after the midsection ($x/L = -0.5$) of Ahmed's body with various afterbody shapes in order to reduce overall computational cost. Therefore, the inlet of the computational domain was located at the midsection ($x/L = -0.5$) of the body and boundary conditions were specified from the previously reported full domain calculations.[5] The three velocity components and the turbulent kinetic energy and its dissipation rate were specified at the inlet and at the outer boundaries from the full domain calculations. The exit plane was located at roughly two body lengths downstream of the body and the constant pressure boundary condition was imposed. Symmetry boundary conditions were enforced at the symmetry plane. At the body surface and the ground lane, no-slip boundary conditions were imposed. Near the wall, the standard log-law wall functions were used for the velocity distribution.[9]

Computational Grid and Performance

A simple sheared grid system was generated by applying algebraic stretching with a hyperbolic tangent function. The previous grid refinement study[5] was presented that established a $97 \times 51 \times 31$ mesh as sufficient for producing grid-independent solutions for the entire body. In the present work, the computations were performed only after the midsection of the body, a $61 \times 51 \times 31$ mesh, was utilized to simulate the flow around the afterbody and the downstream wake. It takes about 200 flow-solver iterations to converge the aerodynamic drag coefficient within an accuracy of 5×10^{-4}. It is estimated that the CPU time per point and iteration (on the CRAY YMP), including data input/output, is about 6×10^{-5} s. Therefore, it takes roughly 30 min of CPU time for one complete calculation of an afterbody with a $61 \times 51 \times 31$ mesh.

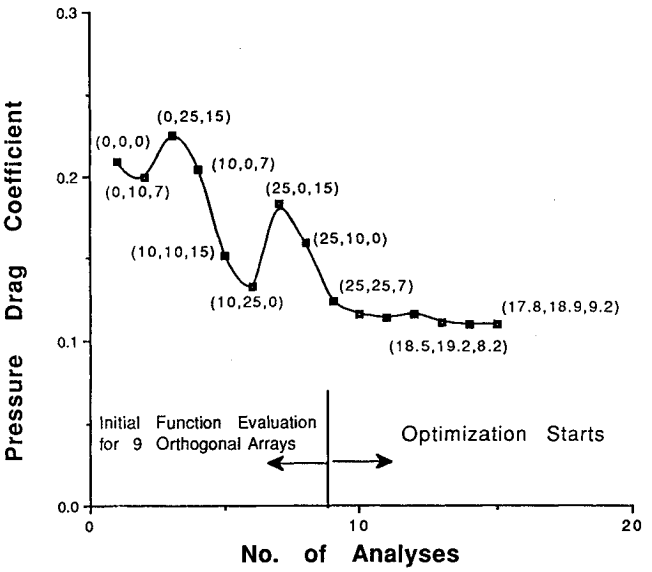

Fig. 2 Convergence history of the pressure drag coefficient with the number of Navier-Stokes analyses (the numbers within the parentheses are the three boat-tail angles α, β, and γ).

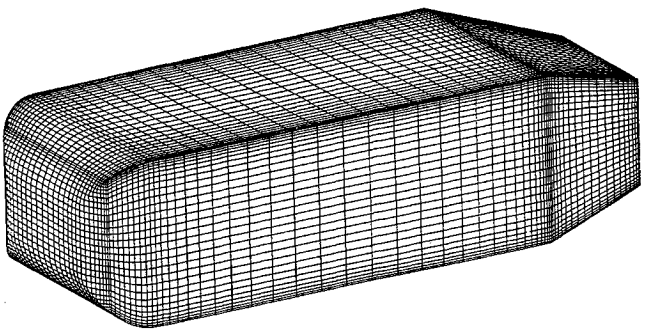

Fig. 3 Surface grid distribution ($97 \times 51 \times 31$) on Ahmed's body with three boat-tail angles ($\alpha = 17.8$, $\beta = 18.9$, $\gamma = 9.2$).

Results and Discussion

The search for the optimum afterbody shape was terminated when the differences of drag coefficient between consecutive iterations were less than 0.001. Among the nine orthogonal arrays, case 9 ($\alpha = 25$, $\beta = 25$, $\gamma = 7$) produced a minimum pressure drag coefficient of 0.124. Optimization started with this afterbody shape as a nominal design after the initial nine function evaluations to establish the quadratic approximation of the drag coefficent. Six additional Navier-Stokes analyses were required to reach an optimum afterbody ($\alpha = 17.8$, $\beta = 18.9$, $\gamma = 9.2$), which reduced the drag coefficient by 0.014. The overall convergence pattern is shown in Fig. 2. The body shape is shown as a surface grid in Fig. 3. The predicted drag coefficient reduction was 0.115 from case 3 ($\alpha = 0$, $\beta = 25$, $\gamma = 15$). The experimentally determined optimum for a similar body indicated a very wide range: 15- –18-deg backlight, 15- –22-deg boat tail, 9- –14-deg ramp. The experimentally measured drag coefficient reduction was 0.13.

Drag and Lift Variations

Contributions to pressure drag from backlight C_α, boat tail C_β, ramp C_γ, and vertical rear-end base C_b were calculated by integration of the axial component of the calculated pressure over the individual surfaces. The afterbody lift coefficient was calculated by integrating the vertical component of surface pressure on the slanted surfaces. The drag breakdown for various afterbody shapes is listed in Table 3 along with the afterbody lift coefficient, the base pressure coefficient, and the base area ratio. Major contribution to the total pressure drag comes from the slanted surfaces and vertical base surface of the rear end. For case 1 (so-called squareback), rear-end pressure drag is wholly due to the flat base. The vertical base area decreases with increasing slant angles, but the base pressure increases as do the relative contributions to the drag of the various afterbody surfaces. The exact level of the base pressure is controlled by both the shedding of longitudinal vortices from the body surfaces and the reverse flow separation near the base.

Wake Flow Structure

The structure of the wake is a consequence of the flow around the body and can offer insight into drag-producing mechanisms. The computed flow will be summarized by presenting results in the plane of symmetry and in a transverse plane at one body length downstream. There were dramatic differences in the predicted wake flows for the 15 cases computed, and four will be discussed here.

Case 1 (0, 0, 0)

The wake behind the body is characterized by a large separation zone, as shown in Figs. 4a and 4b. At the symmetry plane, two recirculating vortices are clearly visible and the separation bubble closes at roughly a half-body length downstream of the body. As listed in Table 3, a relatively low base pressure coefficient, −0.209, was predicted due to the large flow separation at the base. The total pressure contours of Fig. 4c show the turbulent wake at one body length downstream; also shown are the thickened turbulent boundary layers formed on the stationary ground plane. The shape of the wake bound-

Table 3 Drag breakdown and lift coefficient for various afterbodies

Case runs	Backlight α	Boat tail β	Ramp γ	C_D Total drag coefficient	Cl Afterbody lift coefficient	$C\alpha$ Backlight drag coefficient	C_β Boat-tail drag coefficient	C_γ Ramp drag coefficient	C_b Base drag coefficient	Cp Base pressure coefficient	Base area ratio
1	0	0	0	0.209	−0.024	0	0	0	0.209	−0.209	1.0
2	0	10	7	0.199	−0.120	0	0.05	0.027	0.122	−0.186	0.657
3	0	25	15	0.225	−0.079	0	0.142	0.041	0.042	−0.146	0.287
4	10	0	7	0.204	−0.095	0.028	0	0.035	0.141	−0.200	0.704
5	10	10	15	0.151	−0.075	0.026	0.039	0.054	0.032	−0.075	0.425
6	10	25	0	0.133	0.011	0.024	0.122	0	−0.013	0.041	0.320
7	25	0	15	0.183	0.005	0.112	0	0.071	0	0	0.319
8	25	10	0	0.159	0.070	0.084	0.039	0	0.036	−0.083	0.433
9	25	25	7	0.124	0.009	0.053	0.078	0.014	−0.021	0.113	0.186
15	17.8	18.9	9.2	0.110	0.004	0.041	0.063	0.021	−0.015	0.053	0.283

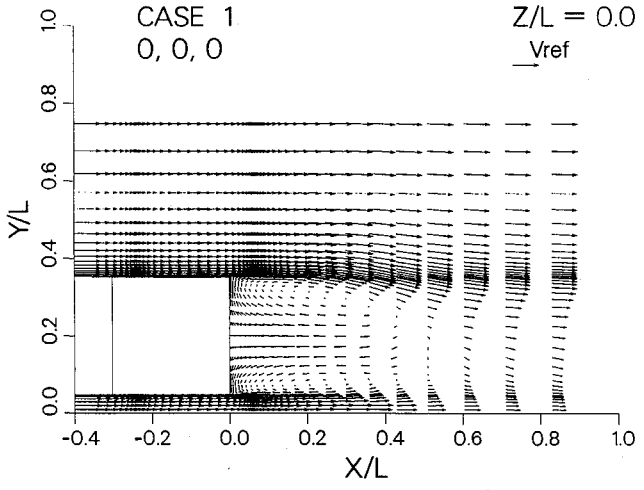

Fig. 4a Velocity vectors in the plane of symmetry for case 1 ($\alpha = 0, \beta = 0, \gamma = 0$).

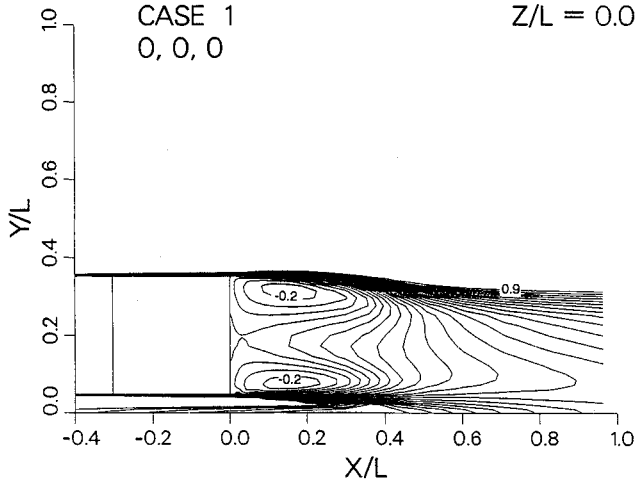

Fig. 4b Total pressure contours in the plane of symmetry for case 1 ($\alpha = 0, \beta = 0, \gamma = 0$).

aries were defined as the position of the 0.9 total pressure contour. The height of the low-energy wake region (total pressure contour 0.3) decreases downstream due to the downwash induced by the weak longitudinal vortices generated downstream of the wake closure, as shown in Fig. 4c. The pair of weak longitudinal vortices was not generated directly from the body surface, but was formed as the result of a slight vorticity imbalance between the upper and the lower vortices shown in Fig. 4a, which are part of a toroidal vortex structure.

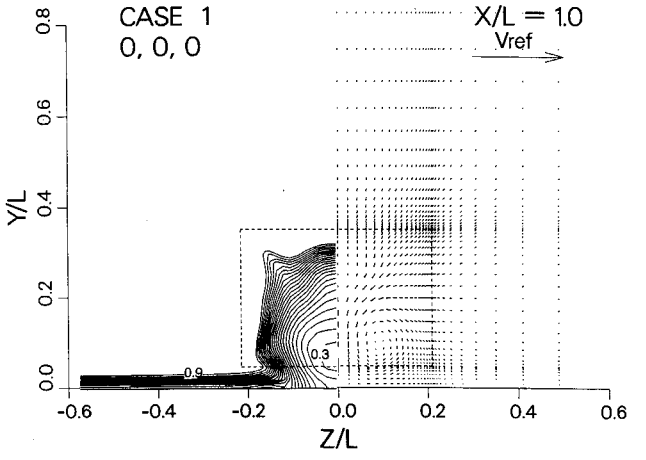

Fig. 4c Total pressure contours and crossflow velocity vectors in the transverse plane at $x/L = 1$ for case 1 ($\alpha = 0, \beta = 0, \gamma = 0$) (dotted lines indicate the body cross section; the base and total pressure contours >0.9 are not shown).

Case 3 (0, 25, 15)

This afterbody shape produced the highest total pressure drag among the 15 afterbody shapes evaluated in the present study, higher even than case 1, which has a constant cross-section afterbody. It is interesting to observe the behavior of the wake at the symmetry plane, as shown in Figs. 5a and 5b. The height of the wake boundary increases rapidly downstream. A pair of strong longitudinal vortices is generated along the upper longitudinal edges and is clearly visible in Fig. 5c. No vortices were formed along the lower longitudinal edges due to a proper match of ramp and boat-tail angles. Because of the strong inflow toward the separation bubble at the rear base, the reverse flow region is relatively short (as shown in Fig. 5a) and narrow (as shown in Fig. 5c).

As shown in Fig. 5c, a sharply defined pair of longitudinal vortices move up and toward each other downstream of the body. This predicted behavior is consistent with the potential theory for vortices in ground proximity.[10] The strong upwash associated with the formation of counter-rotating longitudinal vortices is responsible for the spread of the wake boundaries downstream of the separation bubble. As shown in Figs. 5a and 5b, the height of the wake boundary was extended to roughly two body heights at $x/L = 1.0$. This large wake disturbance is responsible for the high drag coefficient of this afterbody.

Case 9 (25, 25, 7)

This case produced a minimum base area and a minimum pressure drag among the first nine afterbody shapes, which were based on the orthogonal arrays. As shown in Figs. 6a and 6b, the effect of backlight angle tends to dominate the flow pattern in the separation bubble behind the base, and a relatively large upper vortex was generated. No apparent lon-

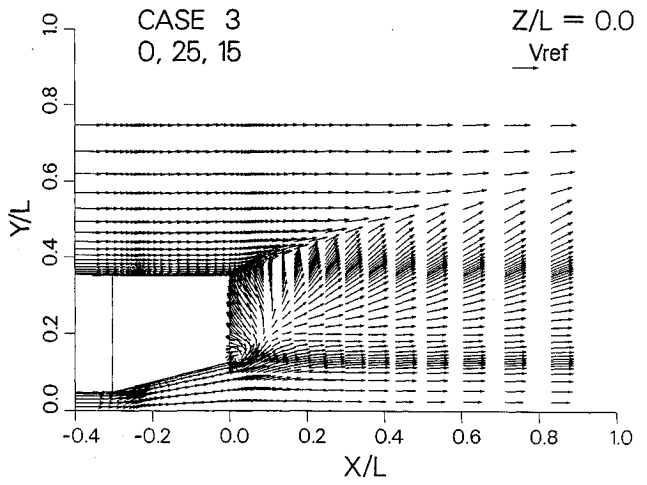

Fig. 5a Velocity vectors in the plane of symmetry for case 3 (α = 0, β = 25, γ = 15).

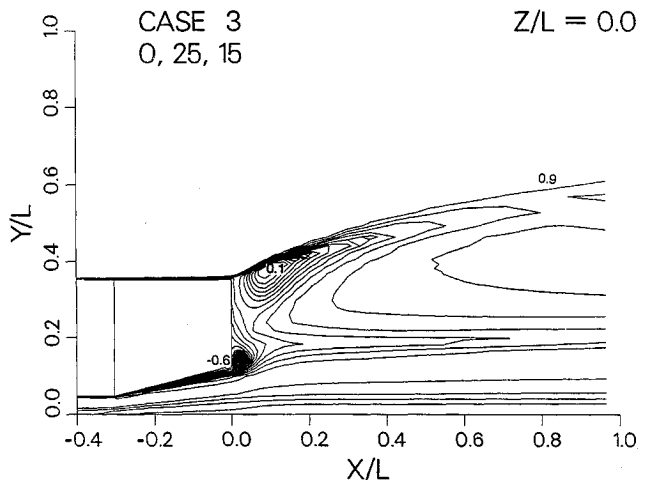

Fig. 5b Total pressure contours in the plane of symmetry for case 3 (α = 0, β = 25, γ = 15).

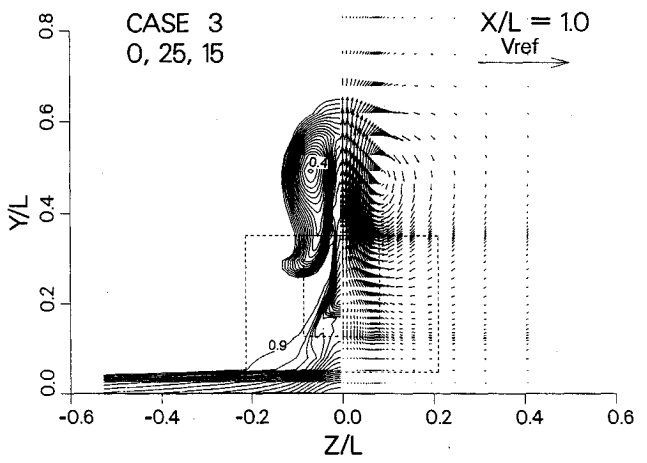

Fig. 5c Total pressure contours and crossflow velocity vectors in the transverse plane at x/L = 1 for case 3 (α = 0, β = 25, γ = 15) (dotted lines indicate the body cross section; the base and total pressure contours >0.9 are not shown).

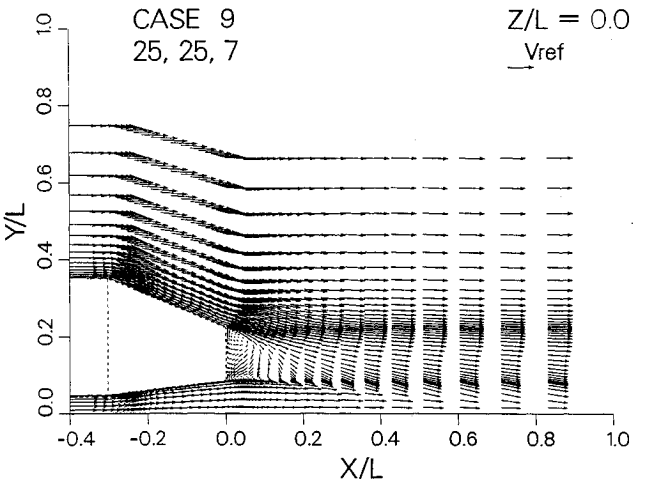

Fig. 6a Velocity vectors in the plane of symmetry for case 9 (α = 25, β = 25, γ = 7).

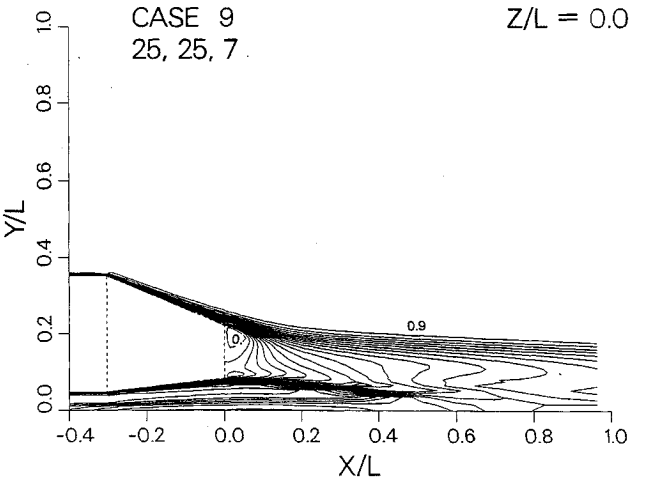

Fig. 6b Total pressure contours in the plane of symmetry for case 9 (α = 25, β = 25, γ = 7).

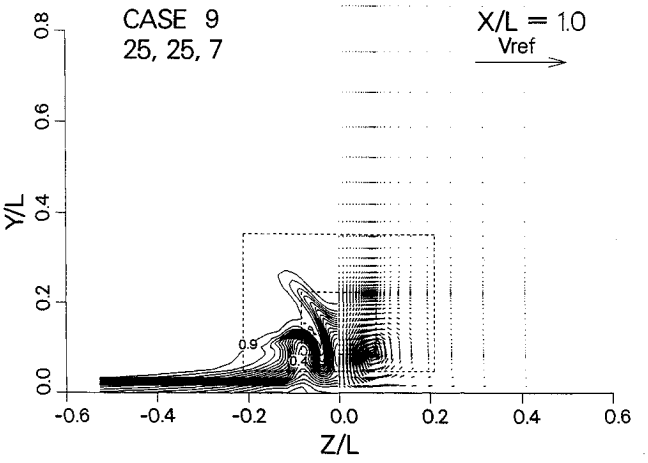

Fig. 6c Total pressure contours and crossflow velocity vectors in the transverse plane at x/L = 1 for case 9 (α = 25, β = 25, γ = 7) (dotted lines indicate the body cross section; the base and total pressure contours >0.9 are not shown).

gitudinal vortices were found along the upper edges. However, a pair of relatively weak vortices was generated along the lower longitudinal edges, as shown in Fig. 6c. These vortices deform the total pressure contours, Fig. 6c; the total pressure contours wrap around the vortex core.

Case 15 (17.8, 18.9, 9.2)

Six additional iterations were performed to obtain this afterbody, which minimized the afterbody pressure drag. This optimum afterbody reduced the overall pressure drag coefficient by 0.115 from case 3 (α = 0, β = 25, γ = 15), and by

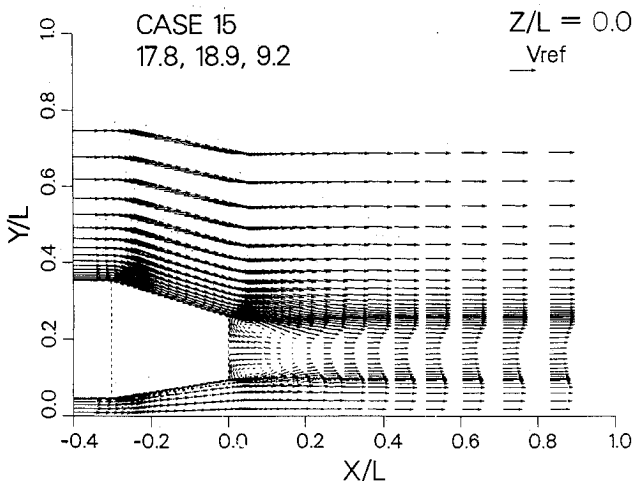

Fig. 7a Velocity vectors in the plane of symmetry for case 15 (α = 17.8, β = 18.9, γ = 9.2).

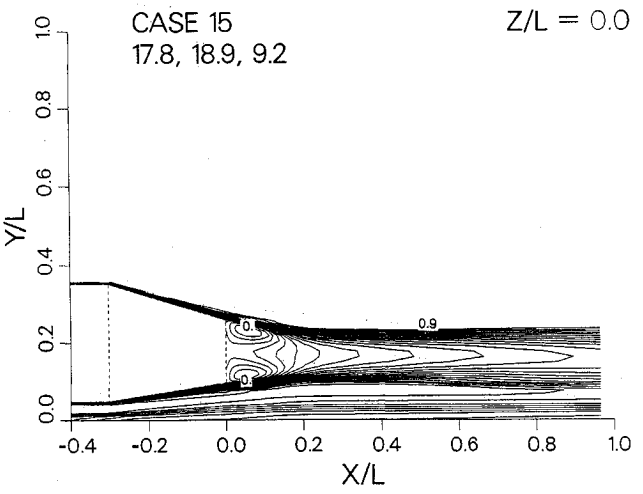

Fig. 7b Total pressure contours in the plane of symmetry for case 15 (α = 17.8, β = 18.9, γ = 9.2).

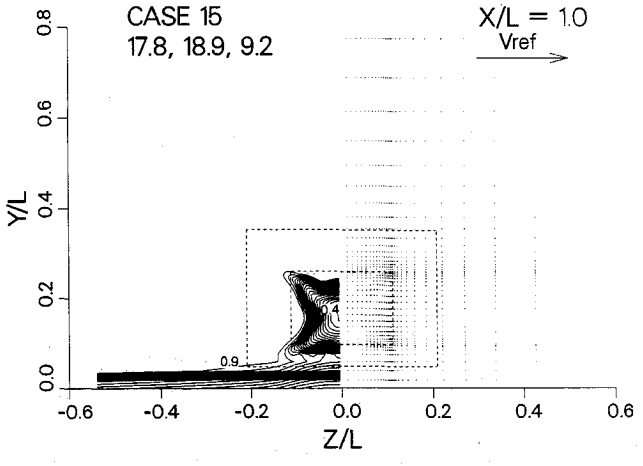

Fig. 7c Total pressure contours and crossflow velocity vectors in the transverse plane at x/L = 1 for case 15 (α = 17.8, β = 18.9, γ = 9.2) (dotted lines indicate the body cross section; the base and total pressure contours >0.9 are not shown).

0.1 from case 1 with the constant afterbody cross section. This body further produced a 0.014 reduction of pressure drag coefficient from case 9 even with a 50% larger base area. The resulting flowfield is characterized by well balanced upper and the lower recirculating vortices in the separation bubble, as shown in Figs. 7a and 7b. This afterbody also minimizes the longitudinal vortices downstream, as shown in Fig. 7c. Previous studies have similarly concluded that minimizing the trailing vortices in the wake will reduce drag.[11,12]

Validation of the Optimization

Data from an independent experimental study can be used to show the qualitative validity of the present computational optimization study. The overall length of the experimental models is 1.44 m and the length:width:height ratios are 3.79:1.38:1.00. Also, the experimental models were equipped with wheels that were mounted with clearance into wheel wells; the afterbody started just downstream of the rear wheel wells. The experiments were carried out in a $^1/_3$-scale wind tunnel at a freestream velocity of 60 m/s, which corresponds to the same unit Reynolds number as the computations. The configuration of the wind tunnel, detailed test procedure, and accuracy of the experimental data are described in a previous paper.[13]

It was observed from computation and experiment that the drag coefficient is very flat near the optimum design variables. A wide range of design parameters (backlight, boat-tail, and ramp angles) near the optimum produces a relatively low afterbody drag coefficient. A quadratic polynomial approximation of the objective function for drag coefficient was obtained from a weighted least-squares fit in which the design information near the optimum are weighted most heavily. This analytic expression for the drag coefficient provides the overall behavior of the drag coefficient near the optimum afterbody shape.

Consider first the comparison of the predicted optimum afterbody geometry to the experimentally determined optimum. Figures 8a–8c show the interactions among three afterbody angles near the optimum afterbody shape. The experimentally determined optimum geometries (15, 15, 9), (18, 18, 9), and (21, 18, 12), have been plotted in Figs. 8a–8c since all three geometries were found to attain the minimum drag of 0.220. The experimentally determined optimums all fall close to the predicted optimum (17.8, 18.9, 9.2). The level of agreement is surprisingly good when the experimental uncertainty of the data (±0.0035) and the differences in the model geometries are considered. The range of the experimentally determined optimum geometries also substantiates the predicted flat nature of the minimum.

The interaction between backlight and ramp angles, as shown in Fig. 8a, makes it necessary to change the backlight angle α and the ramp angle β simultaneously to maintain a relatively low drag coefficient. This is probably because the pair of longitudinal vortices generated from the backlight and the ramp oppose each other and tend to be weakened in strength if the angles are balanced. Figure 8a also shows that a relatively small ramp angle is required to compensate for a relatively large backlight angle. This is due to the stronger vortices formed from the ramp than from the backlight for the same slant angles, α and γ.

The computational and experimental studies are also compared in Figs. 9a–9c, where the incremental changes of afterbody pressure drag coefficient are presented as functions of each of the afterbody parameters using the optimum afterbody value as a reference. As previously discussed, the approximation function for the drag coefficient was obtained from a weighted least-squares fit of the computed drag coefficients of all 15 afterbodies. Since those afterbodies near the optimum were weighted more heavily, the approximation for drag coefficient increments will be most accurate near the optimum afterbody. The experimental data are made up of composites of the available drag data closest to the predicted optimum afterbody geometry. In order to make direct comparisons, both the computational and experimental data were adjusted to give the same value of afterbody pressure drag for the optimum afterbody, case 15. In each comparison, there is good agree-

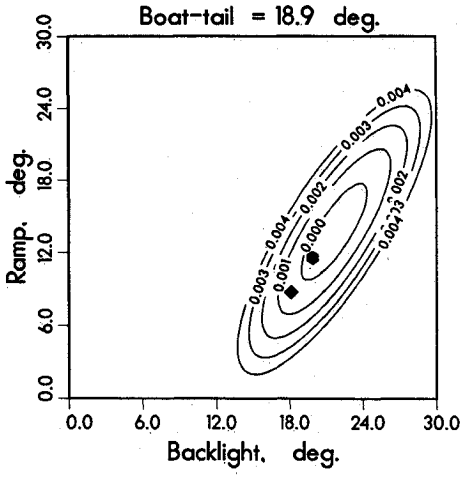

Fig. 8a Iso-contours of the computed afterbody drag coefficient increment near the optimum shape parameters with a fixed boat-tail angle of 18.9 deg and selected experimental data (symbols) for comparison.

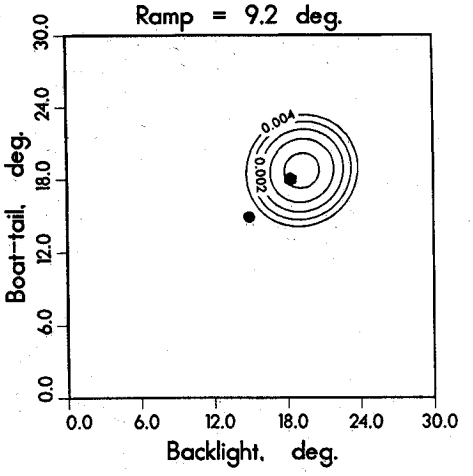

Fig. 8b Iso-contours of the computed afterbody drag coefficient increment near the optimum shape parameters with a fixed ramp angle of 9.2 deg and selected experimental data (symbols) for comparison.

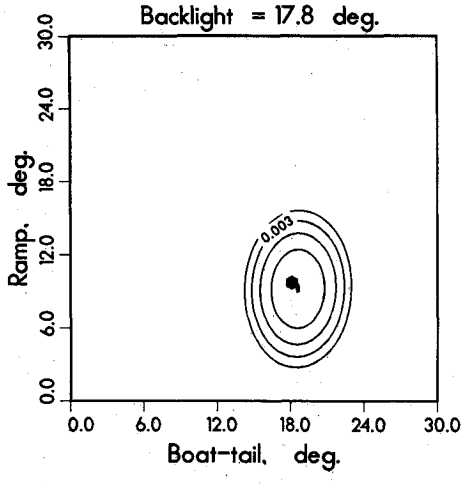

Fig. 8c Iso-contours of the computed afterbody drag coefficient increment near the optimum shape parameters with the fixed backlight angle of 17.8 deg and selected experimental data (symbols) for comparison.

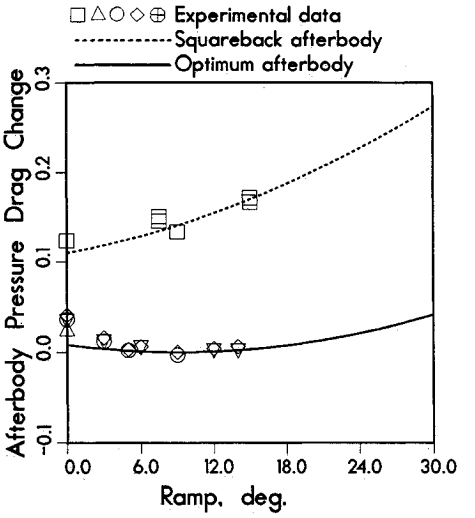

Fig. 9a Computed (lines) and measured (symbols) afterbody drag coefficient change with ramp angle for the optimum (α = 17.8, β = 18.9) and squareback (α = 0, β = 0) afterbodies.

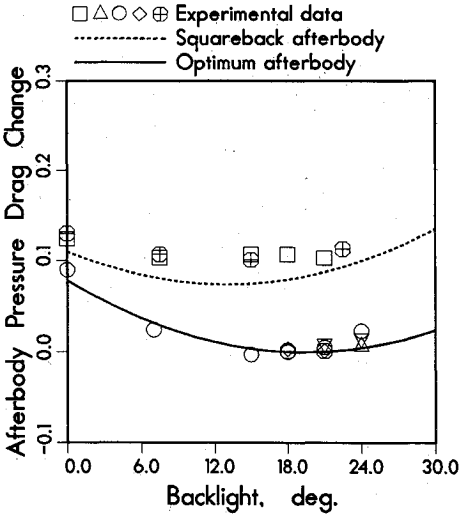

Fig. 9b Computed (lines) and measured (symbols) afterbody drag coefficient change with backlight angle for the optimum (β = 18.9, γ = 9.2) and squareback (β = 0, γ = 0) afterbodies.

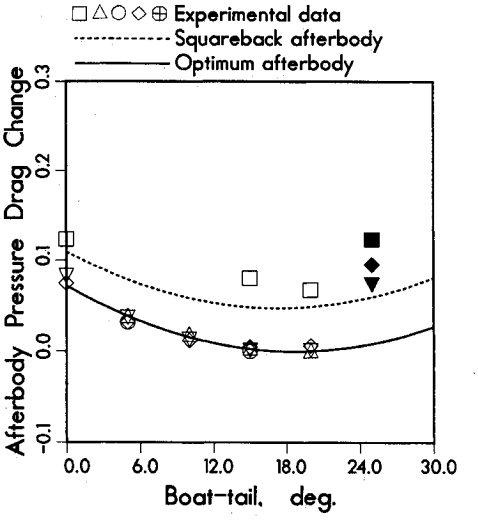

Fig. 9c Computed (lines) and measured (symbols) afterbody drag coefficient change with boat-tail angle for the optimum (α = 17.8, γ = 9.2) and squareback (α = 0, γ = 0) afterbodies.

ment in the shape of the curves, the location of minima, and the drag change from the optimum afterbody (17.8, 18.9, 9.2).

As shown in Fig. 9a, the drag coefficient increases monotonically with the ramp angle for a squareback ($\alpha = 0$, $\beta = 0$), shown as a dotted line, which is substantiated by the experimental data. However, for the optimum afterbody ($\alpha = 17.8$, $\beta = 18.9$), shown as a solid line, the drag coefficient is much less sensitive to the change of the ramp angle. The drag coefficient initially decreases slightly with the ramp angle and then increases gradually after roughly 9 deg of ramp angle. For the optimum afterbody, the weak dependence of the pressure drag on ramp angle was predicted very well, and it agrees with the experimental trend for ramp angles greater than 5 deg.

Figure 9b shows the effects of the backlight angle on the drag coefficients for both squareback ($\beta = 0$, $\gamma = 0$) and the optimum afterbody shapes ($\beta = 18.9$, $\gamma = 9.2$). For the optimum afterbody, shown as a solid line, the drag coefficient initially decreases with increasing backlight angle reaching a minimum near 18 deg of backlight angle. For the squareback, shown as a dotted line, the minimum drag coefficient occurs near 13 deg of backlight angle. As the strength of the longitudinal vortices increases, the drag coefficient starts to increase after 13 deg of backlight angle. The overall trends are consistent with the experimental data, as shown in Fig. 9b.

Figure 9c shows the effects of the boat-tail angle on the drag coefficient. Both the squareback ($\alpha = 0$, $\gamma = 0$) and the optimum afterbody ($\alpha = 17.8$, $\gamma = 9.2$) produced a minimum drag coefficient near 19 deg of boat-tail angle, and the drag coefficient starts to increase for greater angles. The variation of the drag coefficient with boat-tail angle for the optimum afterbody is very well predicted for angles less than 20 deg. However, experimental values increase rapidly beyond 20 deg of boat-tail angle (indicated as filled symbols); this behavior is likely due to flow separation on the boat-tail surfaces, which is thought to occur at approximately 25 deg of boat-tail angle. The k-ϵ turbulence model tends to overpredict skin friction in adverse pressure gradients. It is recognized[14] that the length scale determined by the ϵ equation rises more steeply than experiments near the wall in adverse pressure gradients.

Conclusions

The Navier-Stokes analysis, VINE3D, coupled with the approximate optimization technique produced the optimum afterbody shape with minimum drag that minimizes the longitudinal vortices in the wake and, therefore, afterbody lift coefficient. The present study also recommends to change the backlight angle and the ramp angle simultaneously to maintain a relatively low drag coefficient. The drag data show that the computations correctly predict not only the optimum geometry but also the flat behavior of the drag surface in the vicinity of the minimum. The effects of the backlight angle and the boat-tail angle on the drag coefficient are similar. However, the ramp angle affects the drag coefficient differently. For the ramp angles, the strong longitudinal vortices overpower the boat-tailing effects and the drag coefficient increases monotonically for the squareback afterbody. It has been observed that the strength of the ramp vortices are intensified by the ground plane, which is a unique feature associated with ground vehicles.

References

[1]Morel, T., "Theoretical Lower Limits of Forebody Drag," *Aeronautical Journal*, Paper 639, Jan. 1979, pp. 23–27.

[2]Mair, W. A., "Reduction of Base Drag by Boat-Tailed Afterbodies in Low Speed Flow," *Aeronautical Quarterly*, Vol. 20, 1969, pp. 307–320.

[3]Kohri, L., and Numata, N., "Effects of Rear-End Configuration of Vehicles on Aerodynamic Drag," *International Journal of Vehicle Design*, Vol. 9, No. 2, 1988, pp. 216–224.

[4]Ahmed, S. R., Ramm, G., and Faltin, G., "Some Salient Features of the Time-Averaged Ground Vehicle Wake," Society of Automotive Engineers, Paper 840300, Feb. 1984.

[5]Han, T., "Computational Analysis of Three-Dimensional Turbulent Flow Around a Bluff Body in Ground Proximity," *AIAA Journal*, Vol. 27, No. 9, 1989.

[6]Madsen, L. E., and Vanderplaats, G. N., "COPES—A Fortran Control Program for Engineering Synthesis," Naval Postgraduate School, NPS69-81-003, Monterey, CA, March 1982.

[7]Vanderplaats, G. N., *Numerical Optimization Techniques for Engineering Design*, McGraw-Hill, New York, 1984, pp. 211–215.

[8]Taguchi, G., *Introduction to Quality Engineering*, Asian Productivity Organization, Tokyo, Japan, 1986, pp. 181–188.

[9]Launder, B. E., and Spaulding, D. B., "The Numerical Calculation of Turbulent Flows," *Computational Methods in Applied Mechanics and Engineering*, Vol. 3, March 1974, pp. 269–289.

[10]Teitjens, O. G., *Fundamentals of Hydro- and Aeromechanics*, based on Lectures of L. Prandtl, Dover, New York, 1957, pp. 201–213.

[11]Morelli, A., "Aerodynamic Basic Bodies Suitable for Automobile Applications," *Proceedings of the International Association for Vehicle Design: Technological Advances in Vehicle Design*, SP3, edited by M. A. Dorgham and U. L. Businaro, Interscience Enterprise Ltd., England, UK, 1983.

[12]Bearman, P. W., "Some Observation on Road Vehicle Wakes," Society of Automotive Engineers, Paper 830922, Feb. 1983.

[13]Morel, T., "Aerodynamic Drag of Bluff Body Shapes Characteristics of Hatch-Back Cars," Society of Automotive Engineers, Paper 780267, 1978.

[14]Rodi, W., and Scheuerer, G., "Scrutinizing the k-ϵ Turbulence Model Under Adverse Pressure Gradient Conditions," *Journal of Fluid Engineering*, Vol. 108, 1986, pp. 174–179.